Pressure and temperature dependence of shock remanence intensity for single-domain titanomagnetite-bearing basalt: Toward understanding the magnetic anomalies produced by impact events

Masahiko Sato[1], Kosuke Kurosawa[2], Sunao Hasegawa[3], and Futoshi Takahashi[4]

[1]The University of Tokyo
[2]Chiba Institute of Technology
[3]Japan Aerospace Exploration Agency
[4]Kyushu University

February 20, 2023

Abstract

Knowledge of shock remanent magnetization (SRM) property is crucial for interpreting the spatial change in a magnetic anomaly observed over an impact crater. This study conducted two series of impact-induced SRM acquisition experiments by varying the applied field and impact conditions, and the remanences of cube-shaped subsamples cut from shocked basalt containing single-domain titanomagnetite were measured to investigate the pressure and temperature dependence of the SRM intensity. The peak pressure and peak temperature distributions in the shocked samples were estimated using shock-physics modeling. SRM intensity was proportional to the apple field intensity up to 400 μT. The SRM intensities under different projectile conditions were consistent at the same pressure values. An empirical equation of SRM intensity is proposed to be the power function of pressure and a linear function of temperature, which can express the experimental SRM intensity values in a range of pressures up to 10 GPa and temperatures up to the Curie temperature. The magnetic anomaly estimation over an impact crater was demonstrated using the empirical equation, and the anomaly distribution shows a distinct feature approximated as a combination of two dipoles located at the basement of the crater and a deeper part.

Hosted file

`955970_0_table_10692550_rpsmhv.docx` available at https://authorea.com/users/587557/articles/625171-pressure-and-temperature-dependence-of-shock-remanence-intensity-for-single-domain-titanomagnetite-bearing-basalt-toward-understanding-the-magnetic-anomalies-produced-by-impact-events

Pressure and temperature dependence of shock remanence intensity for single-domain titanomagnetite-bearing basalt: Toward understanding the magnetic anomalies produced by impact events

Masahiko Sato[1]*, Kosuke Kurosawa[2], Sunao Hasegawa[3], and Futoshi Takahashi[4]

[1]Department of Earth and Planetary Science, The University of Tokyo, Tokyo, Japan

[2]Planetary Exploration Research Center, Chiba Institute of Technology, Narashino, Japan

[3]Institute of Space and Astronautical Science, Japan Aerospace Exploration Agency, Sagamihara, Japan

[4]Department of Earth and Planetary Sciences, Kyushu University, Fukuoka, Japan

*Department of Earth and Planetary Science, The University of Tokyo, 7-3-1 Hongo, Bunkyo-ku, Tokyo 113-0033 Japan

Key points

- Two series of shock remanence acquisition and evaluation experiments are conducted by varying applied field and impact conditions.

- An empirical expression for shock remanence intensity is proposed to be the power function of pressure and a linear function of temperature.

- The magnetic anomaly over an impact crater estimated from the empirical equation shows a distinct pattern approximated as two dipoles.

Abstract

Knowledge of shock remanent magnetization (SRM) property is crucial for interpreting the spatial change in a magnetic anomaly observed over an impact crater. This study conducted two series of impact-induced SRM acquisition experiments by varying the applied field and impact conditions, and the remanences of cube-shaped subsamples cut from shocked basalt containing single-domain titanomagnetite were measured to investigate the pressure and temperature dependence of the SRM intensity. The peak pressure and peak temperature distributions in the shocked samples were estimated using shock-physics modeling. SRM intensity was proportional to the apple field intensity up to 400 μT. The SRM intensities under different projectile conditions were consistent at the same pressure values. An empirical equation of SRM intensity is proposed to be the power function of pressure and a linear function of temperature, which can express the experimental SRM intensity values in a range of pressures up to 10 GPa and temperatures up to the Curie temperature. The magnetic anomaly estimation over an impact crater was demonstrated using the empirical equation, and the anomaly distribution shows a distinct feature approximated as a combination of two dipoles located at the basement of the crater and a deeper part.

Plain Language Summary

Knowledge of shock remanence is crucial for interpreting the spatial change in a magnetic anomaly observed over an impact crater and for reconstructing the magnetic field histories of terrestrial planets. This study conducted a suite of shock remanence

acquisition and evaluation experiments to investigate the pressure and temperature dependence of shock remanence intensity. An empirical expression of shock remanence intensity is proposed on the basis of experimental data, and the magnetic anomaly estimation is demonstrated using the proposed empirical equation. The anomaly shows a distinct feature approximated as a combination of two dipoles located at the basement of the crater and a deeper part, and the feature could be used to detect the magnetic anomaly caused by impact events.

1. Introduction

Magnetic anomaly records caused by past impact events play an important role in reconstructing the magnetic field histories of terrestrial planets (Acuña et al., 1999; Halekas et al., 2003; Lillis et al., 2013). At the time of impact events, crustal rocks in terrestrial planets can record shock remanent magnetization (SRM) as a result of shock wave propagation. Knowledge of the spatial distribution of SRM intensity is crucial for interpreting the magnetic anomaly over the impact craters and for reconstructing the paleo-planetary field intensity based on the magnetic field datasets from present observations and future explorations. Nevertheless, the SRM intensity distribution is poorly understood because of the difficulty in evaluating the magnetization distribution within the experimentally SRM-imparted samples. Although post-impact remanence modifications, such as thermoremanent magnetization (TRM) acquisition of a melt sheet (Hood, 2011) and chemical remanent magnetization acquisition due to hydrothermalism (Quesnel et al., 2013), are also important for interpreting crustal remanence distributions, the initial structure of remanent magnetization immediately after the impacts should be explored.

Srnka et al. (1979) qualitatively demonstrated that the SRM intensities decreased with increasing distance from the impact point for multidomain (MD) titanomagnetite-bearing basalt using core samples drilled from a shocked basalt plate. Gattacceca et al. (2008) conducted laser-induced SRM acquisition experiments and remanence measurements of subsamples for pseudo-single-domain (PSD) titanomagnetite-bearing basalt and MD magnetite-bearing microdiorite. The SRM intensities were homogeneous in their experimental samples (Gattacceca et al., 2008), which was further supported by superconducting quantum interference device microscopy measurements for the SRM-bearing basalt (Gattacceca et al., 2010). Sato et al. (2021) established the SRM acquisition method using a two-stage light gas gun and the remanence evaluation method for divided subsamples, and systematic spatial changes in SRM intensity and stability were observed for a single-domain (SD) titanomagnetite-bearing basalt cylinder. Although the spatial changes in SRM intensities were qualitatively evaluated and were different for each magnetic mineral in these previous studies, the quantitative evaluation of SRM intensity with respect to the shock wave conditions such as pressure and temperature changes has not yet been obtained, and further investigation is required to quantitatively understand the relationship between the magnetic anomaly observation data and the crustal remanence originating from the impact event.

Using a magnetically well-characterized basalt sample bearing fine-grained SD titanomagnetite, the SRM acquisition experiments, remanence measurements for cube-shaped subsamples cut from the SRM-imparted samples, and impact simulations were conducted for quantitatively investigating the pressure and temperature dependence of SRM intensity. In one series of experiments, impact experiments were conducted under magnetic fields of 100–400 μT at a nearly constant impact velocity, whereas in the other series of experiments, the impact velocities were set to 1.3–7.0 km/s with different projectiles and a constant applied field value. The peak pressure and peak temperature distributions after the impacts were estimated using shock-physics modeling. Based on the results of the remanence measurements and modeling, we propose an empirical relationship between the SRM intensity and peak pressure/temperature in impact events. In addition, we calculated the magnetic anomaly profile over an impact crater using the empirical equation.

2. Method

A natural basalt sample (Linxi, Inner Mongolia) was used for the experiments. The basalt samples were the same as those used for the SRM experiments in the study by Sato et al. (2021), and the detailed rock magnetic properties have been reported in a previous study. The basalt sample contained SD titanomagnetite with a Curie temperature of 237°C (Sato et al., 2021). Cylindrical basalt samples with a diameter and length of 8 cm were used as targets in the SRM acquisition experiments. The cylindrical basalt samples were subjected to a three-axial alternating field demagnetization (AFD) of 80 mT using a DEM-8601C AF demagnetizer (Natsuhara-Giken) before the SRM acquisition experiments.

Two-stage light-gas guns (vertical and horizontal) at the Institute of Space and Astronautical Science (ISAS) of the Japan Aerospace and Exploration Agency (JAXA) were used for SRM acquisition experiments. This study follows the method employed by Sato et al. (2021). The basalt cylinder, solenoid coil, and magnetic shield were placed coaxially in a vacuum experimental chamber. An aluminum sphere with a diameter of 2 mm and a polycarbonate sphere with a diameter of 7 mm were used as the projectiles, and a nylon slit sabot was used to accelerate the projectile (Kawai et al., 2010). The impact angle was fixed at 90°, measured from the top flat surface of the basalt cylinder, that is, vertical impacts. Two series of experiments were conducted (Table 1). In one series of experiments, impact experiments were conducted under magnetic fields of 100, 150, 200, and 400 μT with nearly constant impact velocities of 5.3–5.5 km/s. In the other series of experiments, the magnetic field was fixed at 100 μT, and the impact velocities were set to 1.3 (polycarbonate), 2.7, 4.0, 5.3, and 7.0 km/s (aluminum).

After the impact experiments on SRM acquisition, the target samples were cut into cube-shaped subsamples approximately 3 mm in length using rock cutters. The subsamples are denoted as *R*i*Z*j, where the indices i and j are the numbers from the impact point in the radial and axial directions of a cylindrical sample. The measured subsamples are listed in Table 2. Remanence measurements were conducted using a superconducting quantum interference device magnetometer (Model 755, 2G Enterprise) at the University of Tokyo. This study followed the method of Sato et al. (2015) for small-sample measurements. The cube-shaped subsample was set at the edge of a rod made of polylactic acid using a double-sided tape. The remanence of the polylactic acid rod was measured before and after sample measurement, and the average remanence of the rod was subtracted to calculate the sample moment. Stepwise AFD treatments of up to 80 mT were conducted using an alternating field demagnetizer (DEM-95C, Natsuhara-Giken) with a two-axis tumbling system. After the stepwise AFD measurements of the SRM state, several samples were selected for each cylindrical sample, and the anhysteretic remanent magnetization (ARM) with DC and AC fields of 100 μT and 80 mT, respectively, were measured to normalize the effect of heterogeneity of magnetic minerals. Additionally, stepwise thermal demagnetization (THD) treatments up to 320°C were conducted on eight cube samples selected from one cylindrical basalt sample using a thermal demagnetizer (TDS-1, Natsuhara-Giken).

A series of impact simulations using a two-dimensional version of the iSALE shock physics code (Amsden et al., 1980; Ivanov et al., 1997; Wünnemann et al., 2006) was conducted to estimate the peak pressure P_{peak} and peak temperature T_{peak} values in the SRM acquisition experiments. This study followed the impact simulations of Sato et al. (2021), and the details of the impact simulation are described in their paper. The impact velocities and shapes of the projectile and target in the simulation were set to the same values as those in the SRM acquisition experiments. The mass-weighted averaged values of P_{peak} and T_{peak} in each 3 mm cube region were calculated to compare the calculated peak pressures and peak temperatures with the experimentally measured SRM properties.

3. Results

The experimental results for an aluminum sphere with a diameter of 2 mm and an impact velocity of 7 km/s (cylindrical basalt samples 3767 and 3769) are summarized in Figures 1–3. The SRM component was calculated as $\boldsymbol{J}_{\mathrm{SRM}}(2) - \boldsymbol{J}_{\mathrm{SRM}}(80)$ and the stability of the SRM component was evaluated as $|\boldsymbol{J}_{\mathrm{SRM}}(6) - \boldsymbol{J}_{\mathrm{SRM}}(80)|/|\boldsymbol{J}_{\mathrm{SRM}}(2) - \boldsymbol{J}_{\mathrm{SRM}}(80)|$, where $\boldsymbol{J}_{\mathrm{SRM}}(X)$ is the SRM vector at the X mT AFD step. The basalt sample acquired SRM and the SRM properties were systematically change with increasing the distance from impact point as observed in Sato et al. (2021): (1) The SRM component is a single component in one direction in the orthogonal vector plots (Figure 1). (2) The SRM intensity systematically changes with distance in the case with an applied field of 100 μT, and the SRM intensity in the case with an applied field of 100 μT is larger than that of the zero field (Figure 2), indicating that the basalt sample acquired remanent magnetization as a result of shock wave propagation in the applied magnetic field. (3) The SRM intensity systematically changed with distance from the impact point (Figure 2). (4) The SRM stability with respect to the AFD treatment systematically changed with distance from the impact point, and the median destructive field of the SRM components was less than 20 mT (Figure 3).

The experimental results for cylindrical basalt samples with different sizes and the same projectile condition (aluminum sphere with a diameter of 2 mm and impact velocity of approximately 7 km/s) are compared in Figure 4. The diameters and lengths of the basalt samples were 8 cm (this study) and 10 cm (Sato et al., 2021), respectively. To normalize the heterogeneity of magnetic minerals among the cylindrical basalt samples, the SRM intensity was normalized as $|\boldsymbol{J}_{\mathrm{SRM}}(2) - \boldsymbol{J}_{\mathrm{SRM}}(80)|/J_{\mathrm{ARM}}$, where J_{ARM} is the average ARM intensity for several cube samples. The 10 cm basalt cylinder sample shows a systematic change in the normalized SRM intensity with approximately 0.1 dispersion at the same P_{peak} value. The changes in the normalized SRM intensity with respect to P_{peak} for the 8 cm basalt cylinder were consistent with those of the 10 cm basalt cylinder within 3–4 cm from the impact point, while the SRM intensity for the 8 cm cylinder deviated from the trend for the 10 cm cylinder beyond 3–4 cm from the impact point. This deviation likely arose from the arrival of an expansion wave from the side of the cylinder, where a free surface exists. Although the effects of sudden pressure release due to the expansion wave from the side surface are not yet fully understood, the geometry is largely different from that of natural impact events. Consequently, we decided to use only the SRM data within 3 cm from the impact point where the pressure release occurred because of the expansion wave from the top surface.

The results of the stepwise THD treatments in the case of an aluminum sphere with a diameter of 2 mm and an impact velocity of 5.3 km/s (cylindrical basalt sample 835) are summarized in Figures 5 and 6. The SRM component was a single component in one direction in the orthogonal vector plot (Figure 5), similar to the stepwise AFD treatments (Figure 1). In contrast to the AFD treatment, the SRM stability with respect to the THD treatment was almost unchanged with the distance from the impact point (Figure 6).

The experimental results in the case of an aluminum sphere with a diameter of 2 mm and nearly-identical impact velocity (5.3–5.5 km/s) and varying the applied field intensity (cylindrical basalt samples 835, 838, 839, and 840) are shown in Figures 7a and 7b. The SRM intensity was normalized as $\{|\boldsymbol{J}_{\mathrm{SRM}}(2) - \boldsymbol{J}_{\mathrm{SRM}}(80)|/B_{\mathrm{SRM}}\}/(J_{\mathrm{ARM}}/B_{\mathrm{ARM}})$, where B_{SRM} and B_{ARM} are the applied DC field intensities for the SRM and ARM, respectively. The normalized SRM intensities and SRM stabilities at 150, 200, and 400 μT showed similar values over the entire pressure range. The normalized SRM intensity and SRM stability values in the cases of 100 μT slightly deviated from the trends of higher field intensities below ~0.5 and ~1 GPa, respectively. These deviations increased with decreasing pressure. These deviations indicate that the SRM properties below ~1 GPa were saturated above 100 μT field conditions. Despite slight saturation, the normalized SRM intensity and SRM stability values were similar in the four cylindrical samples (Figure 7b); thus, the SRM intensity was proportional to the applied field intensity up to 400 μT.

The experimental results for an applied field intensity of 100 μT and various projectile conditions (cylindrical basalt samples 835, 836, 837, 3767, and 3773) are shown in Figures 7c and 7d. The SRM intensity increased with increasing P_{peak} value and deviated from the increasing trend near the impact point owing to the significant temperature increase for each cylindrical sample (Figure 7c). The deviation from this trend becomes significant above 310 K (Figure 8). Comparing the regions with the increasing trend, the SRM intensities for the different projectile conditions were almost consistent at the same P_{peak} values, although the SRM intensities of the slowest aluminum projectile velocity samples were slightly higher than those of the other samples (Figure 7c). The SRM stability systematically increased with increasing P_{peak} value, even in the case T_{peak} values above 310 K, and all basalt cylinder samples showed a consistent trend

(Figure 7d).

4. Discussion

The SRM intensity approximated as linear and power functions of the P_{peak} value for cube samples with T_{peak} below 310 K are shown in Figure 7c. The difference between the linear regression line and experimental data was significant below 0.2 GPa, while the experimental data agreed well with the power function for the entire P_{peak} range (Figure 7c). The SRM intensity dependence on T_{peak} value is assumed to be a linear function because the T_{peak} variations in the experimental data are sparse compared to the P_{peak} variations. The root mean square of the differences between the estimated value and the experimental value were 0.065 and 0.043 for linear and power functions of the P_{peak}, respectively. Thus, this study proposes a power function as an empirical expression for the SRM intensity dependence on P_{peak} value, and the SRM intensity J_{SRM} was approximated for the entire P_{peak} and T_{peak} ranges as

$$\frac{J_{\mathrm{SRM}}}{J_{\mathrm{ARM}}} = 7.09 \times 10^{-1} \times \left(\frac{P_{\mathrm{peak}}}{\mathrm{GPa}}\right)^{0.134} - 1.19 \times 10^{-3} \left(\frac{T_{\mathrm{peak}}}{\mathrm{K}}\right) \quad (1).$$

The experimental and modeled SRM intensities are compared in Figure 9. The intensity differences between the experimental and model values were smaller than the SRM intensity values over the entire P_{peak} and T_{peak} ranges.

The efficiencies of TRM and ARM acquisition for the basalt sample were 46.0 and 12.0 $\mathrm{Am^2kg^{-1}T^{-1}}$, respectively, and the SRM acquisition efficiency with respect to TRM is expressed as

$$\frac{J_{\mathrm{SRM}}}{J_{\mathrm{TRM}}} = 1.85 \times 10^{-1} \times \left(\frac{P_{\mathrm{peak}}}{\mathrm{GPa}}\right)^{0.134} - 3.10 \times 10^{-4} \left(\frac{T_{\mathrm{peak}}}{\mathrm{K}}\right) \text{ (2),}$$

where J_{TRM} is the TRM intensity. Additionally, the law of proportionality of the remanence intensity to the applied field intensity was almost satisfied for the SRM in this study. Then, the empirical SRM intensity relationship with respect to the applied field intensities B, P_{peak}, and T_{peak} is given as

$$J_{\mathrm{SRM}} = \left\{1.85 \times 10^{-1} \times \left(\frac{P_{\mathrm{peak}}}{\mathrm{GPa}}\right)^{0.134} - 3.10 \times 10^{-4} \left(\frac{T_{\mathrm{peak}}}{\mathrm{K}}\right)\right\} \times J_{\mathrm{TRM}}(B_0) \times \frac{B}{B_0} \text{ (3),}$$

where $J_{\mathrm{TRM}}(B_0)$ is the TRM intensity at the acquisition field of B_0.

Based on the empirical equation, we estimated the magnetic anomaly profile over an impact crater on basaltic crust containing SD titanomagnetite. Given that the SD titanomagnetite grains contained in the basaltic crust are identical to those in our experimental sample, the empirical equation for SRM acquisition can be applied to the basaltic crust. The P_{peak} and T_{peak} distributions in the basaltic crust were calculated using the iSALE shock-physics code (Figures 10c and 10d). Details of the shock physics modeling are provided in the Supporting Information. The P_{peak} and T_{peak} values were substituted into the empirical equation (2), and the crustal remanence intensity with respect to the TRM intensity was calculated for the basaltic crust. The crustal rock near the impact point experiences a high temperature during and after the shock wave propagation and should acquire TRM. Then, the TRM values were allocated to the crustal rocks with T_{peak} values above the Curie temperature of titanomagnetite (510 K). The magnetic field was vertically applied to the basaltic crust, and the crustal rock acquired TRM and SRM parallel to the applied field. Because our empirical relationship cannot evaluate the effects of lithostatic pressure and geotherm, zero pressure and uniform temperature in the basaltic crust were assumed to be the initial conditions, which correspond to the craters produced on a laboratory scale. Nevertheless, our simulation may provide a qualitative understanding of the magnetic anomaly profile above the magnetized crater immediately after impact.

The distribution of the crustal remanence is illustrated in Figure 10b. A thin layer of approximately one projectile radius (R_p) around the impact point acquired a strong remanence as TRM, and a vast region outside the TRM layer (20–30 R_p) acquired a significant SRM intensity (>0.05 J_{TRM}). Consequently, the magnetic anomaly at an altitude comparable to the crater diameter (20 R_p) showed a broader distribution with respect to the crater shape (Figure 10a). The contributions of the TRM and SRM regions to the magnetic anomaly are evaluated in Figure 10a. The contribution of the SRM region is three times higher than that of the TRM layer at the center of the crater. These contributions can be approximated as dipole moments located at depths of 10 R_p and 43 R_p for the TRM and SRM regions, respectively. The intensity of latter dipole is ten times larger than that of former. The depth of 43 R_p corresponds to the P_{peak} value of approximately 0.1 GPa and the SRM intensity of 0.04–0.05 J_{TRM}. The remanence intesnsity decreases with increasing the distance from the impact point in the SRM region, and the volume of the same distance area increases with increasing the distance. As the result, an effective center of dipole locates at the depth of 43 R_p. While the remanence intensity at the SRM region is smaller than that of TRM, the volume of SRM region is significantly larger than that of TRM, resulting in the large contribution to the magnetic anomaly. This distinct feature of the anomaly expressed as the two dipoles located at the basement of the crater and a deeper part could be used to detect the magnetic anomaly caused by impact events and would play an important role in reconstructing the magnetic field histories of terrestrial planets. However, a more systematic study based on impact simulations under various conditions and these magnetic anomaly calculations are required to further evaluate the detectability of impact magnetization events on terrestrial planets.

5. Conclusion

This study conducted two series of SRM acquisition experiments varying applied fields and projectile conditions and the remanence measurements for cube-shaped subsamples were conducted for the cylindrical basalt samples containing SD titanomagnetite. The normalized SRM intensity and SRM stability values were similar in the experiments with varying applied fields, and the SRM intensity was proportional to the apple field intensity up to 400 μT. The SRM intensities for different projectile conditions were almost consistent at the same P_{peak} values. Then, the empirical expression for SRM intensity is proposed to be the power function of P_{peak} and a linear function of T_{peak}, which can be used to express the experimental SRM intensity values in the ranges P_{peak} up to 10 GPa and T_{peak} up to the Curie temperature. This empirical equation can be used to estimate the magnetic anomaly distribution over an impact crater. The anomaly showed a distinct feature approximated as two dipoles located at the basement of the crater and a deeper part, and this feature could be used to detect the magnetic anomaly caused by impact events.

Data Availability Statement

Data from this paper are archived at the UTokyo Repository (Sato, 2023). The iSALE shock physics code is not fully open-source, but is distributed on a case-by-case basis to academic users in the impact community for non-commercial use. A description of the application requirements can be found at the iSALE website (https://isale-code.github.io/terms-of-use.html). The M-ANEOS package is available from Thompson et al. (2019). The list of input parameters for the iSALE computations can be found in the Supplementary Information.

Acknowledgement

This study was performed under the collaborative research program with the Hypervelocity Impact Facility (former name: Space Plasma Laboratory), ISAS, JAXA. The authors thank the developers of iSALE, including G. Collins, K. Wünnemann, B. Ivanov, J. Melosh, and D. Elbeshausen. We used pySALEplot to analyze the output file of iSALE, and also thank Tom Davison for the development of pySALEPlot. This study was supported by JSPS KAKENHI grants JP21H01140. K.K. is supported by JSPS KAKENHI grant JP18KK0092 and JP19H00726. K.K. and M.S. are supported by JSPS KAKENHI grant JP21K18660.

References

1. Acuña, M. H., Connerney, J. E. P., Lin, R. P., Mitchell, D., Carlson, C. W., McFadden, J., et al. (1999). Global distribution of crustal magnetization discovered by the Mars Global Surveyor MAG/ER experiment. Science, 284(5415), 790–793.
2. Amsden, A., Ruppel, H., and Hirt, C. (1980). SALE: A simplified ALE computer

program for fluid flow at all speeds, Los Alamos National Laboratories Report, LA-8095:101p.

3. Dunlop, D. J., & Özdemir, Ö. (1997). Rock magnetism: Fundamentals and frontiers, (p. 573). Cambridge University Press.

4. Gattacceca, J., L. Berthe, M. Boustie, F. Vadeboin, P. Rochette, and T. De Resseguier (2008), On the efficiency of shock magnetization processes, Phys. Earth Planet. Inter., 166, 1–10.

5. Gattacceca, J., M. Boustie, E. Lima, B. P. Weiss, T. de Resseguier, and J.-P. Cuq-Lelandais (2010), Unraveling the simultaneous shock magnetization and demagnetization of rocks, Phys. Earth Planet. Inter., 182, 42–49.

6. Halekas, J. S., R. P. Lin, and D. L. Mitchell (2003), Magnetic fields of lunar multi-ring impact basins, Meteorit. Planet. Sci., 38, 565–578.

7. Hood, L. L. (2011), Central magnetic anomalies of Nectarian-aged lunar impact basins: Probable evidence for an early core dynamo, Icarus, 211, 1109–1128.

8. Ivanov, B. A., Deniem, D., and Neukum, G. (1997). Implementation of dynamic strength models into 2-D hydrocodes: Applications for atmospheric breakup and

impact cratering. International Journal of Impact Engineering, 20(1–5), 411–430.

9. Kawai, N., K. Tsurui, S. Hasegawa, and E. Sato (2010), Single microparticle launching method using two-stage light-gas gun for simulating hypervelocity impacts of micrometeoroids and space debris, Rev. Sci. Instrum., 81, 115105.
10. Lillis, R. J., Robbins, S., Manga, M., Halekas, J. S., & Frey, H. V. (2013). Time history of the Martian dynamo from crater magnetic field analysis. Journal of Geophysical Research: Planets, 118, 1488–1511.
11. Néel, L. (1949), Théorie du traînage magnétique des ferromagnétiques en grains fins avec applications aux terres cuites, Ann. Geophys., 5, 99–136.
12. Quesnel, Y., J. Gattacceca, G. R. Osinski, and P. Rochette (2013), Origin of the central magnetic anomaly at the Haughton impact structure, Canada, Earth Planet. Sci. Lett., 367, 116–122.
13. Sato, M. (2023). Data in “Pressure and temperature dependence of shock remanence intensity for single-domain titanomagnetite-bearing basalt: Toward understanding the magnetic anomalies produced by impact events”. Retrieved from http://hdl.handle.net/2261/0002006019.

14. Sato, M., Kurosawa, K., Kato, S., Ushioda, M., & Hasegawa, S. (2021), Shock remanent magnetization intensity and stability distributions of single-domain titanomagnetite-bearing basalt sample under the pressure range of 0.1–10 GPa. Geophysical Research Letters, 48, e2021GL092716.
15. Sato, M., S. Yamamoto, Y. Yamamoto, Y. Okada, M. Ohno, H. Tsunakawa, and S. Maruyama (2015), Rock-magnetic properties of single zircon crystals sampled from the Tanzawa tonalitic pluton, central Japan, Earth Planets Space, 67, 150.
16. Srnka, L., G. Martelli, G. Newton, S. Cisowski, M. Fuller, and R. Schaal (1979), Magnetic field and shock effects and remanent magnetization in a hypervelocity impact experiment, Earth Planet. Sci. Lett., 42, 127–137.
17. Wünnemann, K., Collins, G. S., and Melosh, H. J. (2006). A strain-based porosity model for use in hydrocode simulations of impacts and implications for transient crater growth in porous targets. Icarus, 180(2), 514–527.

Figure 1. Orthogonal vector plots for stepwise alternating field demagnetization of shock remanence (cylindrical basalt sample 3767). Closed and open symbols denote projections

for X–Y and X–Z planes, respectively.

Figure 2. Shock remanence intensity plotted as a function of distance from the impact point (cylindrical basalt samples 3767 and 3769).

Figure 3. Stepwise alternating field demagnetization curves for shock remanences (cylindrical basalt sample 3767). Normalized remanence intensity is plotted as a function of peak alternating field.

Figure 4. Shock remanence intensity plotted as a function of peak pressure during the shock wave propagation. Closed and open black circles denote the data of this study (cylindrical basalt sample 3767) within and beyond 3 cm from impact point, respectively. Grey circles denote the data in Sato et al. (2021).

Figure 5. Orthogonal vector plots for stepwise thermal demagnetization of shock remanence (cylindrical basalt sample 835). Closed and open symbols denote projections

for X–Y and X–Z planes, respectively.

Figure 6. Stepwise thermal demagnetization curves for shock remanences (cylindrical basalt sample 835). Normalized remanence intensity is plotted as a function of peak heating temperature.

Figure 7. Shock remanence (SRM) intensity (a) and stability (b) are plotted as a function of peak pressure during the shock wave propagation for the cylindrical basalt samples 835, 838, 839, and 840. The SRM intensity was calculated as $(J_{\mathrm{SRM}}/B_{\mathrm{SRM}})/(J_{\mathrm{ARM}}/B_{\mathrm{ARM}})$, where the J_{SRM}, J_{ARM}, B_{SRM}, and B_{ARM} are the SRM intensity, anhysteretic remanence intensity, applied field intensity in SRM experiment, and applied DC field intensity in ARM experiment. The shock remanence stability was calculated as $|\boldsymbol{J}_{\mathrm{SRM}}(6) - \boldsymbol{J}_{\mathrm{SRM}}(80)|/|\boldsymbol{J}_{\mathrm{SRM}}(2) - \boldsymbol{J}_{\mathrm{SRM}}(80)|$, where $\boldsymbol{J}_{\mathrm{SRM}}(X)$ is the SRM vector at the X mT AFD step. SRM intensity (c) and stability (d) are plotted as a function of peak pressure during the shock wave propagation for the cylindrical basalt samples 835, 836, 837, 3767, and 3773. The SRM intensity was calculated as $J_{\mathrm{SRM}}/J_{\mathrm{ARM}}$. Black and gray lines in (c) are the linear

regression and power function lines, respectively.

Figure 8. Shock remanent magnetization (SRM) intensity (a and c) and stability (b and d) are plotted as a function of peak temperature during the shock wave propagation (cylindrical basalt samples 835, 836, 837, 3767, and 3773). The SRM intensity was calculated as $|\boldsymbol{J}_{\mathrm{SRM}}(2) - \boldsymbol{J}_{\mathrm{SRM}}(80)|/|\boldsymbol{J}_{\mathrm{ARM}} - \boldsymbol{J}_{\mathrm{ARM}}(80)|$, where the $\boldsymbol{J}_{\mathrm{SRM}}$ and $\boldsymbol{J}_{\mathrm{ARM}}$ are the SRM and anhysteretic remanence vectors, respectively, and the numbers in parentheses indicate peak amplitude of alternating field demagnetization treatments. The shock remanence stability was calculated as $|\boldsymbol{J}_{\mathrm{SRM}}(6) - \boldsymbol{J}_{\mathrm{SRM}}(80)|/|\boldsymbol{J}_{\mathrm{SRM}}(2) - \boldsymbol{J}_{\mathrm{SRM}}(80)|$.

Figure 9. (a) Relationship between the experimental and model SRM intensities. (b) Differences between the experimental and model SRM intensity. Sizes of symbols indicate the magnitude of residual values.

Figure 10. (a) Amplitudes of crustal magnetic fields at an altitude of 20 projectile radius (R_{p}). Two-dimensional maps for (b) crustal remanence intensity, (c) peak pressure during

the shock wave propagation, and (d) peak temperature during the shock wave propagation. The remanence intensity of shock remanence (SRM) is normalized with respect to that of thermal remanent magnetization (TRM). The vertical and radial distances in the two-dimensional maps are normalized with respect to R_p.

Figure 1.

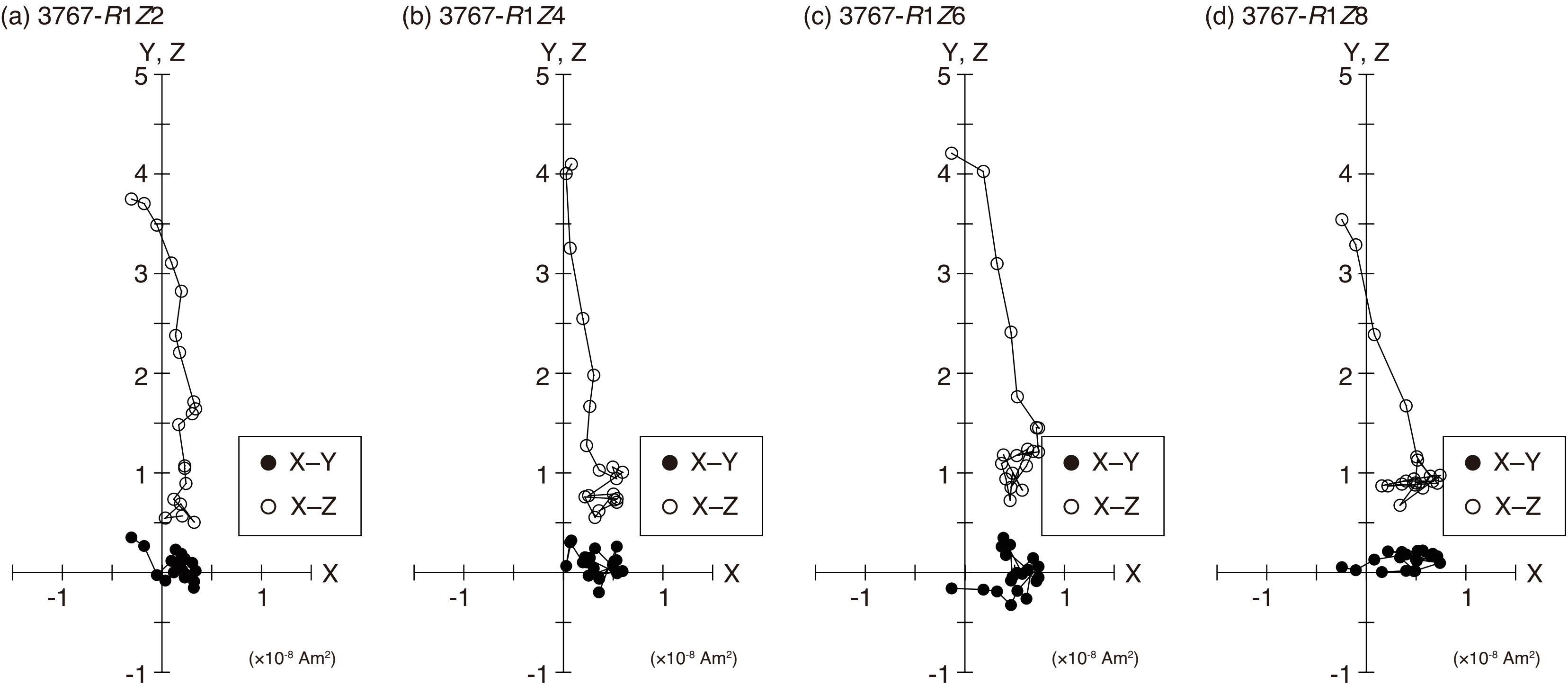
(a) 3767-R1Z2
(b) 3767-R1Z4
(c) 3767-R1Z6
(d) 3767-R1Z8
Y, Z
X
X–Y
X–Z
(×10-8 Am2)
5
4
3
2
1
-1
1

Figure 2.

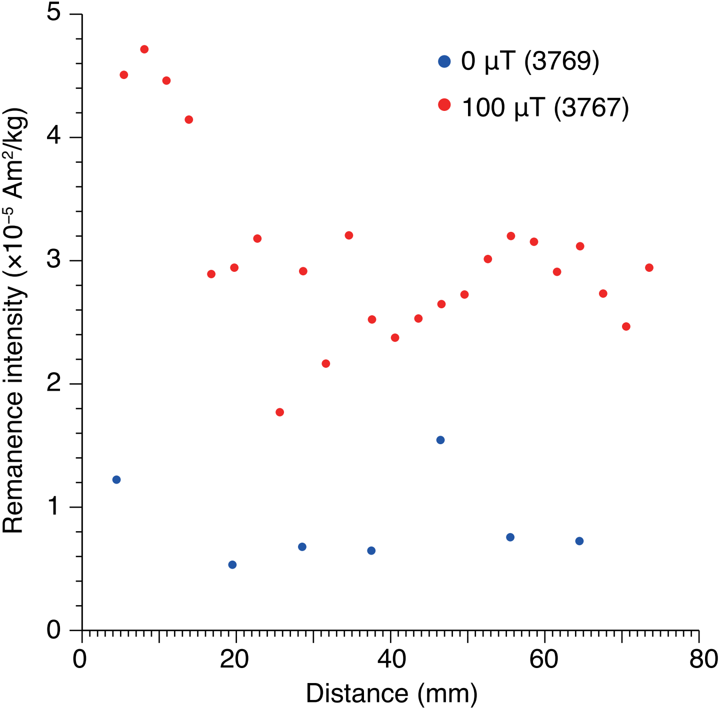

0 μT (3769)
100 μT (3767)
Remanence intensity (×10⁻⁵ Am²/kg)
Distance (mm)
0
1
2
3
4
5
0
20
40
60
80

Figure 3.

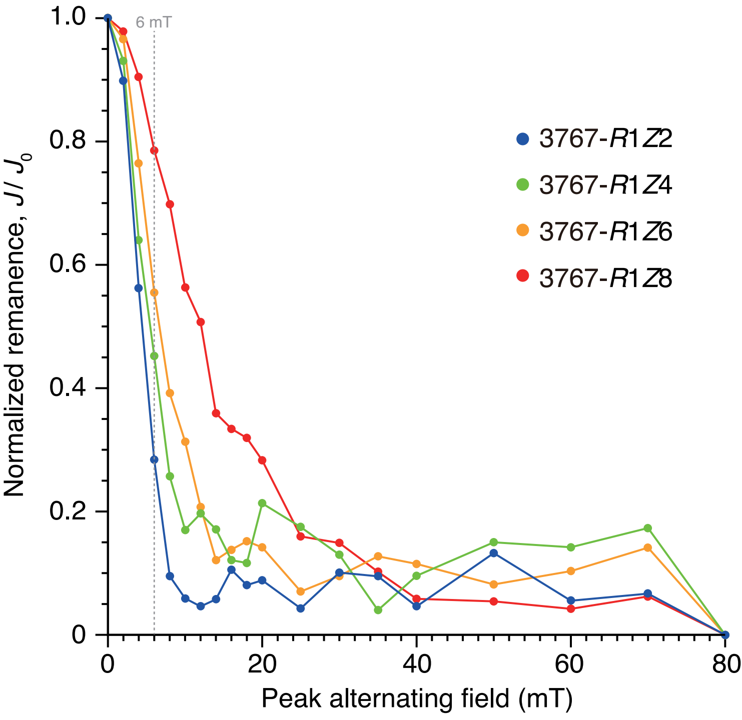

6 mT
1.0
0.8
0.6
0.4
0.2
0
Normalized remanence, J/J_0
0
20
40
60
80
Peak alternating field (mT)
3767-*R*1*Z*2
3767-*R*1*Z*4
3767-*R*1*Z*6
3767-*R*1*Z*8

Figure 4.

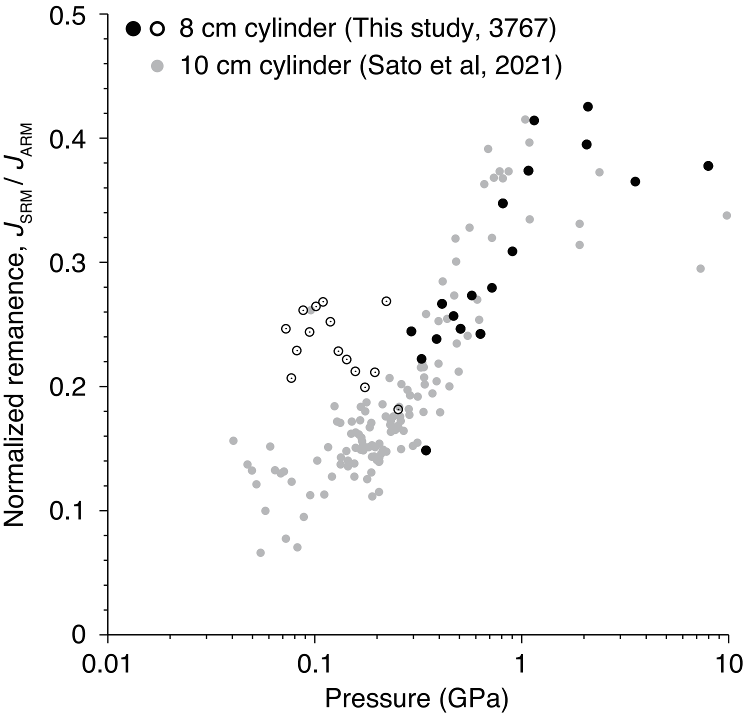

8 cm cylinder (This study, 3767)
10 cm cylinder (Sato et al, 2021)
Normalized remanence, J_{SRM} / J_{ARM}
Pressure (GPa)
0
0.1
0.2
0.3
0.4
0.5
0.01
0.1
1
10

Figure 5.

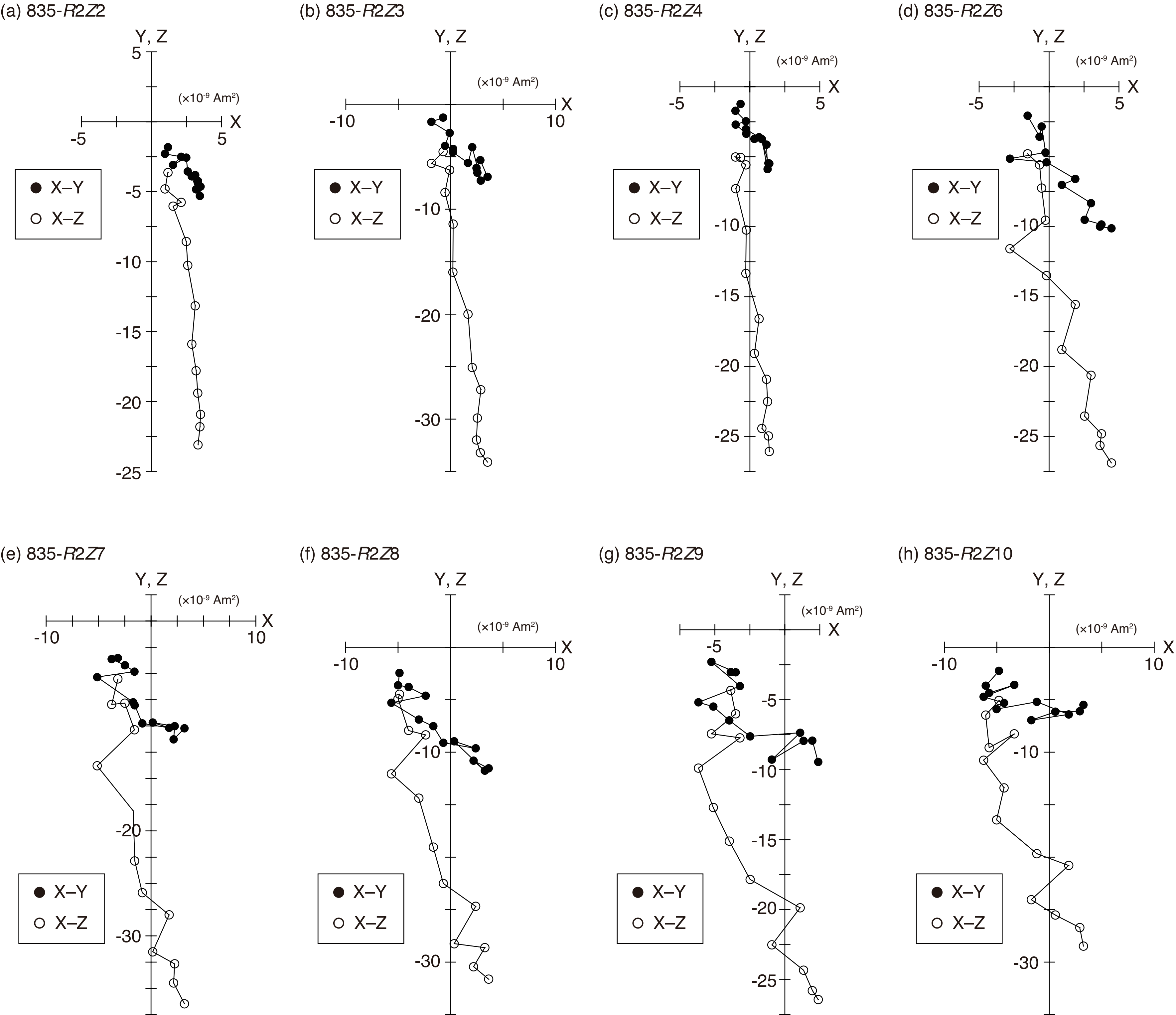

(a) 835-*R2Z*2
(b) 835-*R2Z*3
(c) 835-*R2Z*4
(d) 835-*R2Z*6
(e) 835-*R2Z*7
(f) 835-*R2Z*8
(g) 835-*R2Z*9
(h) 835-*R2Z*10
Y, Z
X
(×10⁻⁹ Am²)
X–Y
X–Z

Figure 6.

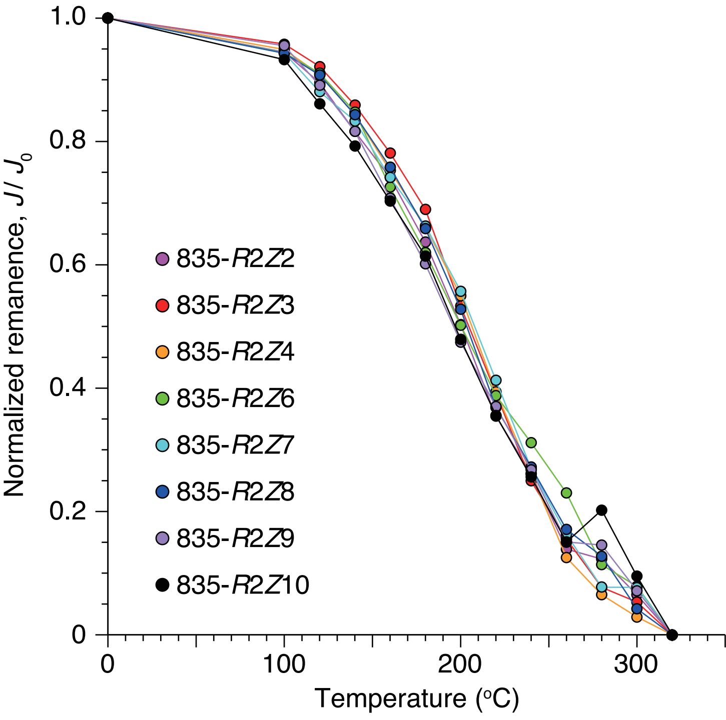

Normalized remanence, J/ J0
Temperature (°C)
835-R2Z2
835-R2Z3
835-R2Z4
835-R2Z6
835-R2Z7
835-R2Z8
835-R2Z9
835-R2Z10
1.0
0.8
0.6
0.4
0.2
0
100
200
300

Figure 7.

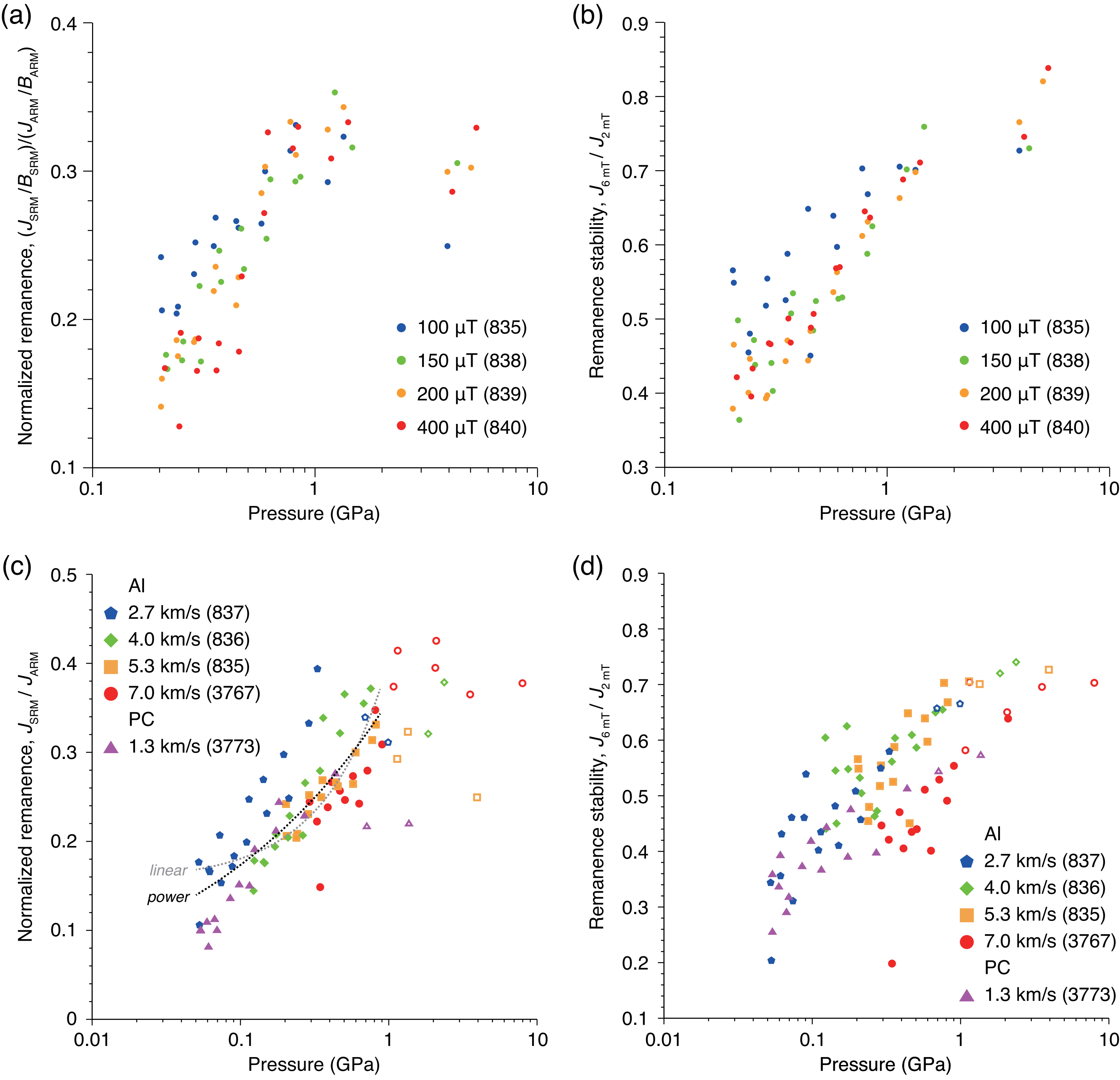

(a)
Normalized remanence, $(J_{SRM}/B_{SRM})/(J_{ARM}/B_{ARM})$
Pressure (GPa)
100 µT (835)
150 µT (838)
200 µT (839)
400 µT (840)
(b)
Remanence stability, $J_{6\,mT}$ / $J_{2\,mT}$
Pressure (GPa)
100 µT (835)
150 µT (838)
200 µT (839)
400 µT (840)
(c)
Normalized remanence, J_{SRM} / J_{ARM}
Pressure (GPa)
Al
2.7 km/s (837)
4.0 km/s (836)
5.3 km/s (835)
7.0 km/s (3767)
PC
1.3 km/s (3773)
linear
power
(d)
Remanence stability, $J_{6\,mT}$ / $J_{2\,mT}$
Pressure (GPa)
Al
2.7 km/s (837)
4.0 km/s (836)
5.3 km/s (835)
7.0 km/s (3767)
PC
1.3 km/s (3773)

Figure 8.

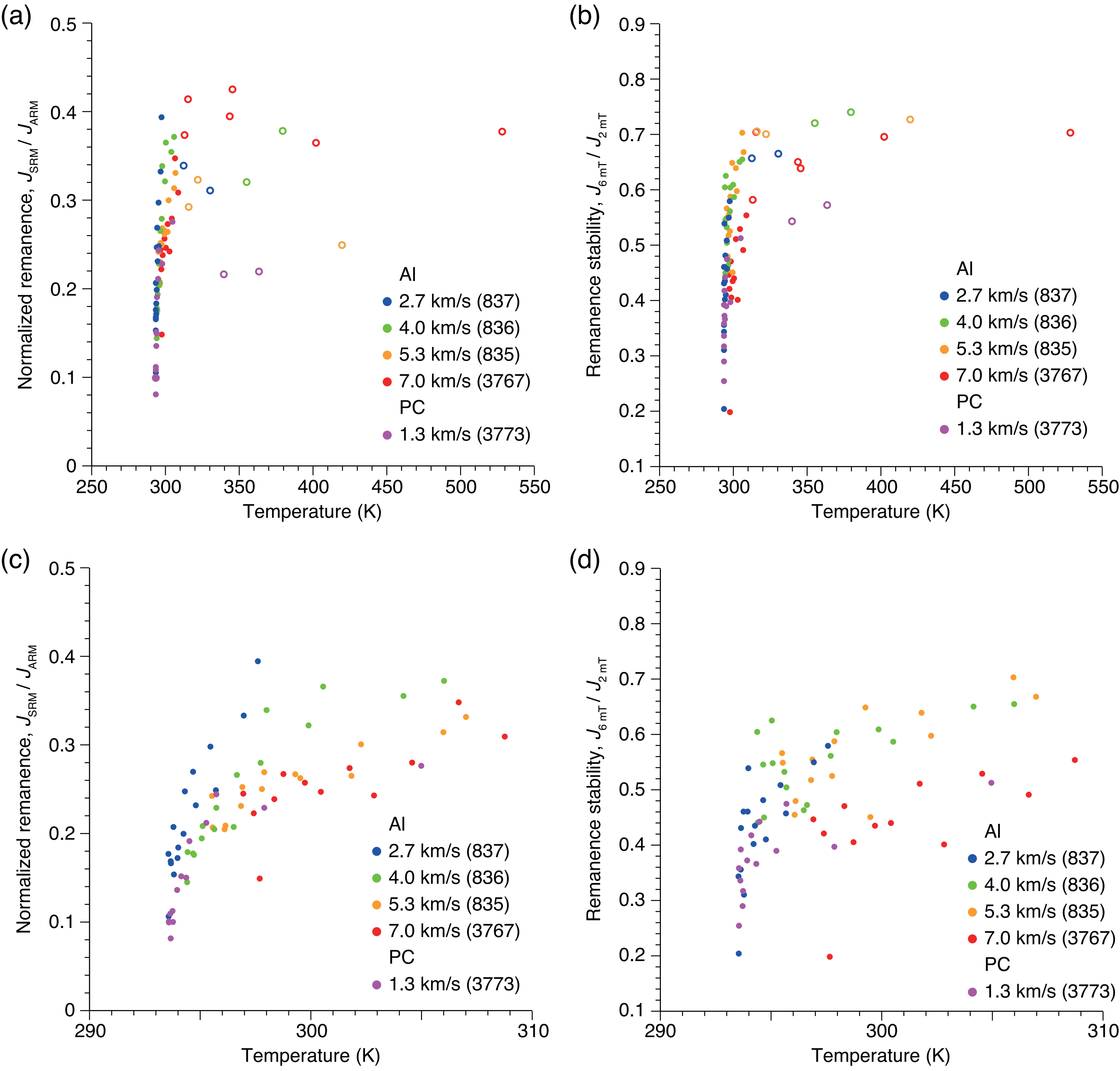

(a)
Normalized remanence, J_{SRM} / J_{ARM}
Temperature (K)
Al
2.7 km/s (837)
4.0 km/s (836)
5.3 km/s (835)
7.0 km/s (3767)
PC
1.3 km/s (3773)
(b)
Remanence stability, $J_{6\,mT}$ / $J_{2\,mT}$
Temperature (K)
Al
2.7 km/s (837)
4.0 km/s (836)
5.3 km/s (835)
7.0 km/s (3767)
PC
1.3 km/s (3773)
(c)
Normalized remanence, J_{SRM} / J_{ARM}
Temperature (K)
Al
2.7 km/s (837)
4.0 km/s (836)
5.3 km/s (835)
7.0 km/s (3767)
PC
1.3 km/s (3773)
(d)
Remanence stability, $J_{6\,mT}$ / $J_{2\,mT}$
Temperature (K)
Al
2.7 km/s (837)
4.0 km/s (836)
5.3 km/s (835)
7.0 km/s (3767)
PC
1.3 km/s (3773)

Figure 9.

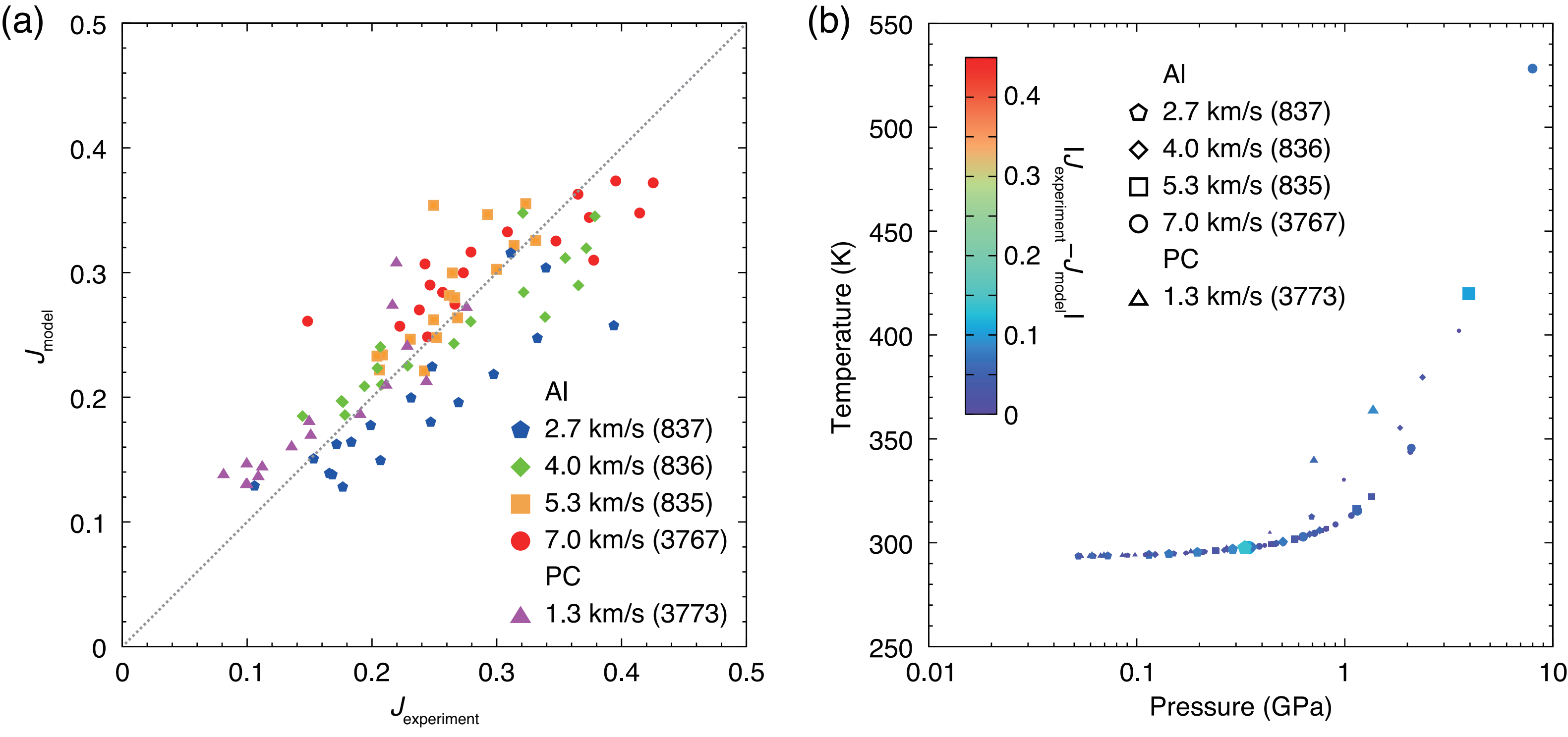
(a)
(b)
J_{model}
$J_{experiment}$
Al
2.7 km/s (837)
4.0 km/s (836)
5.3 km/s (835)
7.0 km/s (3767)
PC
1.3 km/s (3773)
Temperature (K)
Pressure (GPa)
$|J_{experiment}-J_{model}|$
0
0.1
0.2
0.3
0.4
0.5
250
300
350
400
450
500
550
0.01
1
10

Figure 10.

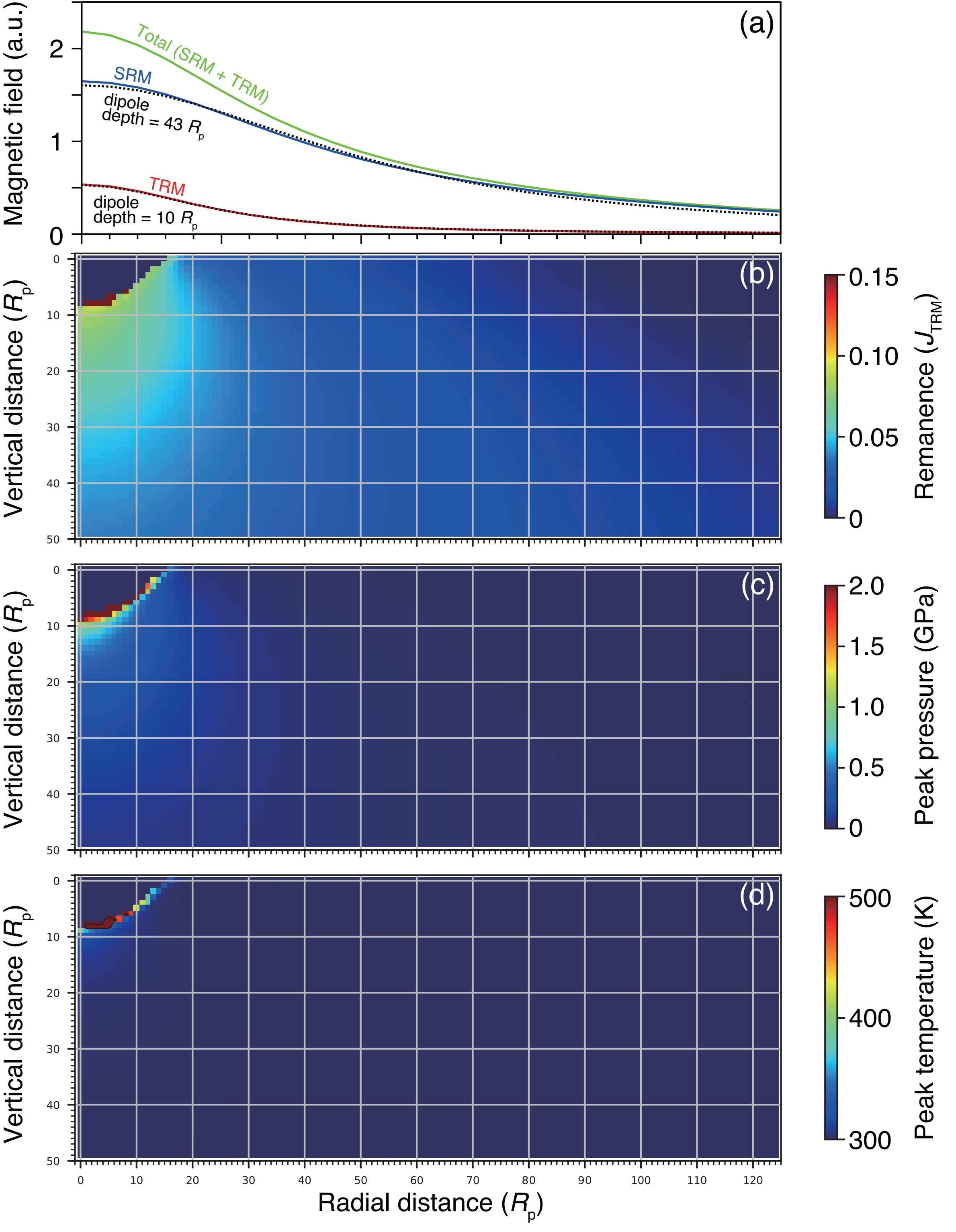

(a)
Total (SRM + TRM)
SRM
dipole
depth = 43 R_p
TRM
dipole
depth = 10 R_p
Magnetic field (a.u.)
(b)
Remanence (J_{TRM})
(c)
Peak pressure (GPa)
(d)
Peak temperature (K)
Vertical distance (R_p)
Radial distance (R_p)

Table 1. Summary of experimental samples

Cylinder ID	Gun-type	Projectile Material/Diameter	Impactor velocity (km/s)	Magnetic field (μT)
835	Vertical	Al 2 mm	5.3	100
836	Vertical	Al 2 mm	4.0	100
837	Vertical	Al 2 mm	2.7	100
838	Vertical	Al 2 mm	5.5	150
839	Vertical	Al 2 mm	5.3	200
840	Vertical	Al 2 mm	5.4	400
3767	Horizontal	Al 2 mm	7.0	100
3769	Horizontal	Al 2 mm	7.0	0
3773	Horizontal	PC 7 mm	1.3	100

Table 2. Summary of shock remanence measurements

Cylinder ID	Cube ID		
	R	*Z*	Treatment
835	1	3–10	AFD at 2 and 80 mT
	2	2–10	AFD at 2 and 80 mT
	2	2–4 and 6–10	THD at 100–320 °C
836	1	2–10	AFD at 2 and 80 mT
	2	2–10	AFD at 2 and 80 mT
837	1	2–10	AFD at 2 and 80 mT
	2	2–10	AFD at 2 and 80 mT
838	1	3–10	AFD at 2 and 80 mT
	2	2–10	AFD at 2 and 80 mT
839	1	2–10	AFD at 2 and 80 mT
	2	2–10	AFD at 2 and 80 mT
840	1	2–10	AFD at 2 and 80 mT
	2	2–10	AFD at 2 and 80 mT
3767	1	2, 4, 6, and 8	AFD at 2–80 mT
	2	2–25	AFD at 2 and 80 mT
	3	1–9	AFD at 2 and 80 mT
3769	1	1, 6, 9, 12, 15, 18, and 21	AFD at 2 and 80 mT
3773	2	1–6, 8, and 9	AFD at 2 and 80 mT
	3	1–9	AFD at 2 and 80 mT

AFD: alternating field demagnetization.

Pressure and temperature dependence of shock remanence intensity for single-domain titanomagnetite-bearing basalt: Toward understanding the magnetic anomalies produced by impact events

Masahiko Sato[1]*, Kosuke Kurosawa[2], Sunao Hasegawa[3], and Futoshi Takahashi[4]

[1]Department of Earth and Planetary Science, The University of Tokyo, Tokyo, Japan

[2]Planetary Exploration Research Center, Chiba Institute of Technology, Narashino, Japan

[3]Institute of Space and Astronautical Science, Japan Aerospace Exploration Agency, Sagamihara, Japan

[4]Department of Earth and Planetary Sciences, Kyushu University, Fukuoka, Japan

*Department of Earth and Planetary Science, The University of Tokyo, 7-3-1 Hongo, Bunkyo-ku, Tokyo 113-0033 Japan

Key points

- Two series of shock remanence acquisition and evaluation experiments are conducted by varying applied field and impact conditions.

- An empirical expression for shock remanence intensity is proposed to be the power function of pressure and a linear function of temperature.

- The magnetic anomaly over an impact crater estimated from the empirical equation shows a distinct pattern approximated as two dipoles.

Abstract

Knowledge of shock remanent magnetization (SRM) property is crucial for interpreting the spatial change in a magnetic anomaly observed over an impact crater. This study conducted two series of impact-induced SRM acquisition experiments by varying the applied field and impact conditions, and the remanences of cube-shaped subsamples cut from shocked basalt containing single-domain titanomagnetite were measured to investigate the pressure and temperature dependence of the SRM intensity. The peak pressure and peak temperature distributions in the shocked samples were estimated using shock-physics modeling. SRM intensity was proportional to the apple field intensity up to 400 μT. The SRM intensities under different projectile conditions were consistent at the same pressure values. An empirical equation of SRM intensity is proposed to be the power function of pressure and a linear function of temperature, which can express the experimental SRM intensity values in a range of pressures up to 10 GPa and temperatures up to the Curie temperature. The magnetic anomaly estimation over an impact crater was demonstrated using the empirical equation, and the anomaly distribution shows a distinct feature approximated as a combination of two dipoles located at the basement of the crater and a deeper part.

Plain Language Summary

Knowledge of shock remanence is crucial for interpreting the spatial change in a magnetic anomaly observed over an impact crater and for reconstructing the magnetic field histories of terrestrial planets. This study conducted a suite of shock remanence acquisition and evaluation experiments to investigate the pressure and temperature dependence of shock remanence intensity. An empirical expression of shock remanence intensity is proposed on the basis of experimental data, and the magnetic anomaly estimation is demonstrated using the proposed empirical equation. The anomaly shows a distinct feature approximated as a combination of two dipoles located at the basement of the crater and a deeper part, and the feature could be used to detect the magnetic anomaly caused by impact events.

1. Introduction

Magnetic anomaly records caused by past impact events play an important role in reconstructing the magnetic field histories of terrestrial planets (Acuña et al., 1999; Halekas et al., 2003; Lillis et al., 2013). At the time of impact events, crustal rocks in terrestrial planets can record shock remanent magnetization (SRM) as a result of shock wave propagation. Knowledge of the spatial distribution of SRM intensity is crucial for interpreting the magnetic anomaly over the impact craters and for reconstructing the paleo-planetary field intensity based on the magnetic field datasets from present observations and future explorations. Nevertheless, the SRM intensity distribution is poorly understood because of the difficulty in evaluating the magnetization distribution within the experimentally SRM-imparted samples. Although post-impact remanence modifications, such as thermoremanent magnetization (TRM) acquisition of a melt sheet (Hood, 2011) and chemical remanent magnetization acquisition due to hydrothermalism (Quesnel et al., 2013), are also important for interpreting crustal remanence distributions, the initial structure of remanent magnetization immediately after the impacts should be explored.

Srnka et al. (1979) qualitatively demonstrated that the SRM intensities decreased with increasing distance from the impact point for multidomain (MD) titanomagnetite-bearing basalt using core samples drilled from a shocked basalt plate. Gattacceca et al. (2008) conducted laser-induced SRM acquisition experiments and remanence measurements of subsamples for pseudo-single-domain (PSD) titanomagnetite-bearing basalt and MD magnetite-bearing microdiorite. The SRM intensities were homogeneous in their experimental samples (Gattacceca et al., 2008), which was further supported by superconducting quantum interference device microscopy measurements for the SRM-bearing basalt (Gattacceca et al., 2010). Sato et al. (2021) established the SRM acquisition method using a two-stage light gas gun and the remanence evaluation method for divided subsamples, and systematic spatial changes in SRM intensity and stability were observed for a single-domain (SD) titanomagnetite-bearing basalt cylinder. Although the spatial changes in SRM intensities were qualitatively evaluated and were different for each magnetic mineral in these previous studies, the quantitative evaluation of SRM intensity with respect to the shock wave conditions such as pressure and temperature changes has not yet been obtained, and further investigation is required to quantitatively understand the relationship between the magnetic anomaly observation data and the crustal remanence originating from the impact event.

Using a magnetically well-characterized basalt sample bearing fine-grained SD titanomagnetite, the SRM acquisition experiments, remanence measurements for cube-shaped subsamples cut from the SRM-imparted samples, and impact simulations were conducted for quantitatively investigating the pressure and temperature dependence of SRM intensity. In one series of experiments, impact experiments were conducted under magnetic fields of 100–400 μT at a nearly constant impact velocity, whereas in the other series of experiments, the impact velocities were set to 1.3–7.0 km/s with different projectiles and a constant applied field value. The peak pressure and peak temperature distributions after the impacts were estimated using shock-physics modeling. Based on the results of the remanence measurements and modeling, we propose an empirical relationship between the SRM intensity and peak pressure/temperature in impact events. In addition, we calculated the magnetic anomaly profile over an impact crater using the empirical equation.

2. Method

A natural basalt sample (Linxi, Inner Mongolia) was used for the experiments. The basalt samples were the same as those used for the SRM experiments in the study by Sato et al. (2021), and the detailed rock magnetic properties have been reported in a previous study. The basalt sample contained SD titanomagnetite with a Curie temperature of 237°C (Sato et al., 2021). Cylindrical basalt samples with a diameter and length of 8 cm were used as targets in the SRM acquisition experiments. The cylindrical basalt samples were subjected to a three-axial alternating field demagnetization (AFD) of 80 mT using a DEM-8601C AF demagnetizer (Natsuhara-Giken) before the SRM acquisition experiments.

Two-stage light-gas guns (vertical and horizontal) at the Institute of Space and Astronautical Science (ISAS) of the Japan Aerospace and Exploration Agency (JAXA) were used for SRM acquisition experiments. This study follows the method employed by Sato et al. (2021). The basalt cylinder, solenoid coil, and magnetic shield were placed coaxially in a vacuum experimental chamber. An aluminum sphere with a diameter of 2 mm and a polycarbonate sphere with a diameter of 7 mm were used as the projectiles, and a nylon slit sabot was used to accelerate the projectile (Kawai et al., 2010). The impact angle was fixed at 90°, measured from the top flat surface of the basalt cylinder, that is, vertical impacts. Two series of experiments were conducted (Table 1). In one series of experiments, impact experiments were conducted under magnetic fields of 100, 150, 200, and 400 μT with nearly constant impact velocities of 5.3–5.5 km/s. In the other series of experiments, the magnetic field was fixed at 100 μT, and the impact velocities were set to 1.3 (polycarbonate), 2.7, 4.0, 5.3, and 7.0 km/s (aluminum).

After the impact experiments on SRM acquisition, the target samples were cut into cube-shaped subsamples approximately 3 mm in length using rock cutters. The subsamples are denoted as *R*i*Z*j, where the indices i and j are the numbers from the impact point in the radial and axial directions of a cylindrical sample. The measured subsamples are listed in Table 2. Remanence measurements were conducted using a superconducting quantum interference device magnetometer (Model 755, 2G Enterprise) at the University of Tokyo. This study followed the method of Sato et al. (2015) for small-sample measurements. The cube-shaped subsample was set at the edge of a rod made of polylactic acid using a double-sided tape. The remanence of the polylactic acid rod was measured before and after sample measurement, and the average remanence of the rod was subtracted to calculate the sample moment. Stepwise AFD treatments of up to 80 mT were conducted using an alternating field demagnetizer (DEM-95C, Natsuhara-Giken) with a two-axis tumbling system. After the stepwise AFD measurements of the SRM state, several samples were selected for each cylindrical sample, and the anhysteretic remanent magnetization (ARM) with DC and AC fields of 100 μT and 80 mT, respectively, were measured to normalize the effect of heterogeneity of magnetic minerals. Additionally, stepwise thermal demagnetization (THD) treatments up to 320°C were conducted on eight cube samples selected from one cylindrical basalt sample using a thermal demagnetizer (TDS-1, Natsuhara-Giken).

A series of impact simulations using a two-dimensional version of the iSALE shock physics code (Amsden et al., 1980; Ivanov et al., 1997; Wünnemann et al., 2006) was conducted to estimate the peak pressure P_{peak} and peak temperature T_{peak} values in the SRM acquisition experiments. This study followed the impact simulations of Sato et al. (2021), and the details of the impact simulation are described in their paper. The impact velocities and shapes of the projectile and target in the simulation were set to the same values as those in the SRM acquisition experiments. The mass-weighted averaged values of P_{peak} and T_{peak} in each 3 mm cube region were calculated to compare the calculated peak pressures and peak temperatures with the experimentally measured SRM properties.

3. Results

The experimental results for an aluminum sphere with a diameter of 2 mm and an impact velocity of 7 km/s (cylindrical basalt samples 3767 and 3769) are summarized in Figures 1–3. The SRM component was calculated as $\boldsymbol{J}_{\mathrm{SRM}}(2) - \boldsymbol{J}_{\mathrm{SRM}}(80)$ and the stability of the SRM component was evaluated as $|\boldsymbol{J}_{\mathrm{SRM}}(6) - \boldsymbol{J}_{\mathrm{SRM}}(80)|/|\boldsymbol{J}_{\mathrm{SRM}}(2) - \boldsymbol{J}_{\mathrm{SRM}}(80)|$, where $\boldsymbol{J}_{\mathrm{SRM}}(X)$ is the SRM vector at the X mT AFD step. The basalt sample acquired SRM and the SRM properties were systematically change with increasing the distance from impact point as observed in Sato et al. (2021): (1) The SRM component is a single component in one direction in the orthogonal vector plots (Figure 1). (2) The SRM intensity systematically changes with distance in the case with an applied field of 100 μT, and the SRM intensity in the case with an applied field of 100 μT is larger than that of the zero field (Figure 2), indicating that the basalt sample acquired remanent magnetization as a result of shock wave propagation in the applied magnetic field. (3) The SRM intensity systematically changed with distance from the impact point (Figure 2). (4) The SRM stability with respect to the AFD treatment systematically changed with distance from the impact point, and the median destructive field of the SRM components was less than 20 mT (Figure 3).

The experimental results for cylindrical basalt samples with different sizes and the same projectile condition (aluminum sphere with a diameter of 2 mm and impact velocity of approximately 7 km/s) are compared in Figure 4. The diameters and lengths of the basalt samples were 8 cm (this study) and 10 cm (Sato et al., 2021), respectively. To normalize the heterogeneity of magnetic minerals among the cylindrical basalt samples, the SRM intensity was normalized as $|\boldsymbol{J}_{\mathrm{SRM}}(2) - \boldsymbol{J}_{\mathrm{SRM}}(80)|/J_{\mathrm{ARM}}$, where J_{ARM} is the average ARM intensity for several cube samples. The 10 cm basalt cylinder sample shows a systematic change in the normalized SRM intensity with approximately 0.1 dispersion at the same P_{peak} value. The changes in the normalized SRM intensity with respect to P_{peak} for the 8 cm basalt cylinder were consistent with those of the 10 cm basalt cylinder within 3–4 cm from the impact point, while the SRM intensity for the 8 cm cylinder deviated from the trend for the 10 cm cylinder beyond 3–4 cm from the impact point. This deviation likely arose from the arrival of an expansion wave from the side of the cylinder, where a free surface exists. Although the effects of sudden pressure release due to the expansion wave from the side surface are not yet fully understood, the geometry is largely different from that of natural impact events. Consequently, we decided to use only the SRM data within 3 cm from the impact point where the pressure release occurred because of the expansion wave from the top surface.

The results of the stepwise THD treatments in the case of an aluminum sphere with a diameter of 2 mm and an impact velocity of 5.3 km/s (cylindrical basalt sample 835) are summarized in Figures 5 and 6. The SRM component was a single component in one direction in the orthogonal vector plot (Figure 5), similar to the stepwise AFD treatments (Figure 1). In contrast to the AFD treatment, the SRM stability with respect to the THD treatment was almost unchanged with the distance from the impact point (Figure 6).

The experimental results in the case of an aluminum sphere with a diameter of 2 mm and nearly-identical impact velocity (5.3–5.5 km/s) and varying the applied field intensity (cylindrical basalt samples 835, 838, 839, and 840) are shown in Figures 7a and 7b. The SRM intensity was normalized as $\{|\boldsymbol{J}_{\mathrm{SRM}}(2) - \boldsymbol{J}_{\mathrm{SRM}}(80)|/B_{\mathrm{SRM}}\}/(J_{\mathrm{ARM}}/B_{\mathrm{ARM}})$, where B_{SRM} and B_{ARM} are the applied DC field intensities for the SRM and ARM, respectively. The normalized SRM intensities and SRM stabilities at 150, 200, and 400 μT showed similar values over the entire pressure range. The normalized SRM intensity and SRM stability values in the cases of 100 μT slightly deviated from the trends of higher field intensities below ~0.5 and ~1 GPa, respectively. These deviations increased with decreasing pressure. These deviations indicate that the SRM properties below ~1 GPa were saturated above 100 μT field conditions. Despite slight saturation, the normalized SRM intensity and SRM stability values were similar in the four cylindrical samples (Figure 7b); thus, the SRM intensity was proportional to the applied field intensity up to 400 μT.

The experimental results for an applied field intensity of 100 μT and various projectile conditions (cylindrical basalt samples 835, 836, 837, 3767, and 3773) are shown in Figures 7c and 7d. The SRM intensity increased with increasing P_{peak} value and deviated from the increasing trend near the impact point owing to the significant temperature increase for each cylindrical sample (Figure 7c). The deviation from this trend becomes significant above 310 K (Figure 8). Comparing the regions with the increasing trend, the SRM intensities for the different projectile conditions were almost consistent at the same P_{peak} values, although the SRM intensities of the slowest aluminum projectile velocity samples were slightly higher than those of the other samples (Figure 7c). The SRM stability systematically increased with increasing P_{peak} value, even in the case T_{peak} values above 310 K, and all basalt cylinder samples showed a consistent trend

(Figure 7d).

4. Discussion

The SRM intensity approximated as linear and power functions of the P_{peak} value for cube samples with T_{peak} below 310 K are shown in Figure 7c. The difference between the linear regression line and experimental data was significant below 0.2 GPa, while the experimental data agreed well with the power function for the entire P_{peak} range (Figure 7c). The SRM intensity dependence on T_{peak} value is assumed to be a linear function because the T_{peak} variations in the experimental data are sparse compared to the P_{peak} variations. The root mean square of the differences between the estimated value and the experimental value were 0.065 and 0.043 for linear and power functions of the P_{peak}, respectively. Thus, this study proposes a power function as an empirical expression for the SRM intensity dependence on P_{peak} value, and the SRM intensity J_{SRM} was approximated for the entire P_{peak} and T_{peak} ranges as

$$\frac{J_{\mathrm{SRM}}}{J_{\mathrm{ARM}}} = 7.09 \times 10^{-1} \times \left(\frac{P_{\mathrm{peak}}}{\mathrm{GPa}}\right)^{0.134} - 1.19 \times 10^{-3} \left(\frac{T_{\mathrm{peak}}}{\mathrm{K}}\right) \text{ (1).}$$

The experimental and modeled SRM intensities are compared in Figure 9. The intensity differences between the experimental and model values were smaller than the SRM intensity values over the entire P_{peak} and T_{peak} ranges.

The efficiencies of TRM and ARM acquisition for the basalt sample were 46.0 and 12.0 $\mathrm{Am^2kg^{-1}T^{-1}}$, respectively, and the SRM acquisition efficiency with respect to TRM is expressed as

$$\frac{J_{\mathrm{SRM}}}{J_{\mathrm{TRM}}} = 1.85 \times 10^{-1} \times \left(\frac{P_{\mathrm{peak}}}{\mathrm{GPa}}\right)^{0.134} - 3.10 \times 10^{-4} \left(\frac{T_{\mathrm{peak}}}{\mathrm{K}}\right) \quad (2),$$

where J_{TRM} is the TRM intensity. Additionally, the law of proportionality of the remanence intensity to the applied field intensity was almost satisfied for the SRM in this study. Then, the empirical SRM intensity relationship with respect to the applied field intensities B, P_{peak}, and T_{peak} is given as

$$J_{\mathrm{SRM}} = \left\{1.85 \times 10^{-1} \times \left(\frac{P_{\mathrm{peak}}}{\mathrm{GPa}}\right)^{0.134} - 3.10 \times 10^{-4} \left(\frac{T_{\mathrm{peak}}}{\mathrm{K}}\right)\right\} \times J_{\mathrm{TRM}}(B_0) \times \frac{B}{B_0} \quad (3),$$

where $J_{\mathrm{TRM}}(B_0)$ is the TRM intensity at the acquisition field of B_0.

Based on the empirical equation, we estimated the magnetic anomaly profile over an impact crater on basaltic crust containing SD titanomagnetite. Given that the SD titanomagnetite grains contained in the basaltic crust are identical to those in our experimental sample, the empirical equation for SRM acquisition can be applied to the basaltic crust. The P_{peak} and T_{peak} distributions in the basaltic crust were calculated using the iSALE shock-physics code (Figures 10c and 10d). Details of the shock physics modeling are provided in the Supporting Information. The P_{peak} and T_{peak} values were substituted into the empirical equation (2), and the crustal remanence intensity with respect to the TRM intensity was calculated for the basaltic crust. The crustal rock near the impact point experiences a high temperature during and after the shock wave propagation and should acquire TRM. Then, the TRM values were allocated to the crustal rocks with T_{peak} values above the Curie temperature of titanomagnetite (510 K). The magnetic field was vertically applied to the basaltic crust, and the crustal rock acquired TRM and SRM parallel to the applied field. Because our empirical relationship cannot evaluate the effects of lithostatic pressure and geotherm, zero pressure and uniform temperature in the basaltic crust were assumed to be the initial conditions, which correspond to the craters produced on a laboratory scale. Nevertheless, our simulation may provide a qualitative understanding of the magnetic anomaly profile above the magnetized crater immediately after impact.

The distribution of the crustal remanence is illustrated in Figure 10b. A thin layer of approximately one projectile radius (R_p) around the impact point acquired a strong remanence as TRM, and a vast region outside the TRM layer (20–30 R_p) acquired a significant SRM intensity (>0.05 J_{TRM}). Consequently, the magnetic anomaly at an altitude comparable to the crater diameter (20 R_p) showed a broader distribution with respect to the crater shape (Figure 10a). The contributions of the TRM and SRM regions to the magnetic anomaly are evaluated in Figure 10a. The contribution of the SRM region is three times higher than that of the TRM layer at the center of the crater. These contributions can be approximated as dipole moments located at depths of 10 R_p and 43 R_p for the TRM and SRM regions, respectively. The intensity of latter dipole is ten times larger than that of former. The depth of 43 R_p corresponds to the P_{peak} value of approximately 0.1 GPa and the SRM intensity of 0.04–0.05 J_{TRM}. The remanence intesnsity decreases with increasing the distance from the impact point in the SRM region, and the volume of the same distance area increases with increasing the distance. As the result, an effective center of dipole locates at the depth of 43 R_p. While the remanence intensity at the SRM region is smaller than that of TRM, the volume of SRM region is significantly larger than that of TRM, resulting in the large contribution to the magnetic anomaly. This distinct feature of the anomaly expressed as the two dipoles located at the basement of the crater and a deeper part could be used to detect the magnetic anomaly caused by impact events and would play an important role in reconstructing the magnetic field histories of terrestrial planets. However, a more systematic study based on impact simulations under various conditions and these magnetic anomaly calculations are required to further evaluate the detectability of impact magnetization events on terrestrial planets.

5. Conclusion

This study conducted two series of SRM acquisition experiments varying applied fields and projectile conditions and the remanence measurements for cube-shaped subsamples were conducted for the cylindrical basalt samples containing SD titanomagnetite. The normalized SRM intensity and SRM stability values were similar in the experiments with varying applied fields, and the SRM intensity was proportional to the apple field intensity up to 400 μT. The SRM intensities for different projectile conditions were almost consistent at the same P_{peak} values. Then, the empirical expression for SRM intensity is proposed to be the power function of P_{peak} and a linear function of T_{peak}, which can be used to express the experimental SRM intensity values in the ranges P_{peak} up to 10 GPa and T_{peak} up to the Curie temperature. This empirical equation can be used to estimate the magnetic anomaly distribution over an impact crater. The anomaly showed a distinct feature approximated as two dipoles located at the basement of the crater and a deeper part, and this feature could be used to detect the magnetic anomaly caused by impact events.

Data Availability Statement

Data from this paper are archived at the UTokyo Repository (Sato, 2023). The iSALE shock physics code is not fully open-source, but is distributed on a case-by-case basis to academic users in the impact community for non-commercial use. A description of the application requirements can be found at the iSALE website (https://isale-code.github.io/terms-of-use.html). The M-ANEOS package is available from Thompson et al. (2019). The list of input parameters for the iSALE computations can be found in the Supplementary Information.

Acknowledgement

This study was performed under the collaborative research program with the Hypervelocity Impact Facility (former name: Space Plasma Laboratory), ISAS, JAXA. The authors thank the developers of iSALE, including G. Collins, K. Wünnemann, B. Ivanov, J. Melosh, and D. Elbeshausen. We used pySALEplot to analyze the output file of iSALE, and also thank Tom Davison for the development of pySALEPlot. This study was supported by JSPS KAKENHI grants JP21H01140. K.K. is supported by JSPS KAKENHI grant JP18KK0092 and JP19H00726. K.K. and M.S. are supported by JSPS KAKENHI grant JP21K18660.

References

1. Acuña, M. H., Connerney, J. E. P., Lin, R. P., Mitchell, D., Carlson, C. W., McFadden, J., et al. (1999). Global distribution of crustal magnetization discovered by the Mars Global Surveyor MAG/ER experiment. Science, 284(5415), 790–793.
2. Amsden, A., Ruppel, H., and Hirt, C. (1980). SALE: A simplified ALE computer

program for fluid flow at all speeds, Los Alamos National Laboratories Report, LA-8095:101p.

3. Dunlop, D. J., & Özdemir, Ö. (1997). Rock magnetism: Fundamentals and frontiers, (p. 573). Cambridge University Press.
4. Gattacceca, J., L. Berthe, M. Boustie, F. Vadeboin, P. Rochette, and T. De Resseguier (2008), On the efficiency of shock magnetization processes, Phys. Earth Planet. Inter., 166, 1–10.
5. Gattacceca, J., M. Boustie, E. Lima, B. P. Weiss, T. de Resseguier, and J.-P. Cuq-Lelandais (2010), Unraveling the simultaneous shock magnetization and demagnetization of rocks, Phys. Earth Planet. Inter., 182, 42–49.
6. Halekas, J. S., R. P. Lin, and D. L. Mitchell (2003), Magnetic fields of lunar multi-ring impact basins, Meteorit. Planet. Sci., 38, 565–578.
7. Hood, L. L. (2011), Central magnetic anomalies of Nectarian-aged lunar impact basins: Probable evidence for an early core dynamo, Icarus, 211, 1109–1128.
8. Ivanov, B. A., Deniem, D., and Neukum, G. (1997). Implementation of dynamic strength models into 2-D hydrocodes: Applications for atmospheric breakup and

impact cratering. International Journal of Impact Engineering, 20(1–5), 411–430.

9. Kawai, N., K. Tsurui, S. Hasegawa, and E. Sato (2010), Single microparticle launching method using two-stage light-gas gun for simulating hypervelocity impacts of micrometeoroids and space debris, Rev. Sci. Instrum., 81, 115105.

10. Lillis, R. J., Robbins, S., Manga, M., Halekas, J. S., & Frey, H. V. (2013). Time history of the Martian dynamo from crater magnetic field analysis. Journal of Geophysical Research: Planets, 118, 1488–1511.

11. Néel, L. (1949), Théorie du traînage magnétique des ferromagnétiques en grains fins avec applications aux terres cuites, Ann. Geophys., 5, 99–136.

12. Quesnel, Y., J. Gattacceca, G. R. Osinski, and P. Rochette (2013), Origin of the central magnetic anomaly at the Haughton impact structure, Canada, Earth Planet. Sci. Lett., 367, 116–122.

13. Sato, M. (2023). Data in “Pressure and temperature dependence of shock remanence intensity for single-domain titanomagnetite-bearing basalt: Toward understanding the magnetic anomalies produced by impact events”. Retrieved from http://hdl.handle.net/2261/0002006019.

14. Sato, M., Kurosawa, K., Kato, S., Ushioda, M., & Hasegawa, S. (2021), Shock remanent magnetization intensity and stability distributions of single-domain titanomagnetite-bearing basalt sample under the pressure range of 0.1–10 GPa. Geophysical Research Letters, 48, e2021GL092716.
15. Sato, M., S. Yamamoto, Y. Yamamoto, Y. Okada, M. Ohno, H. Tsunakawa, and S. Maruyama (2015), Rock-magnetic properties of single zircon crystals sampled from the Tanzawa tonalitic pluton, central Japan, Earth Planets Space, 67, 150.
16. Srnka, L., G. Martelli, G. Newton, S. Cisowski, M. Fuller, and R. Schaal (1979), Magnetic field and shock effects and remanent magnetization in a hypervelocity impact experiment, Earth Planet. Sci. Lett., 42, 127–137.
17. Wünnemann, K., Collins, G. S., and Melosh, H. J. (2006). A strain-based porosity model for use in hydrocode simulations of impacts and implications for transient crater growth in porous targets. Icarus, 180(2), 514–527.

Figure 1. Orthogonal vector plots for stepwise alternating field demagnetization of shock remanence (cylindrical basalt sample 3767). Closed and open symbols denote projections

for X–Y and X–Z planes, respectively.

Figure 2. Shock remanence intensity plotted as a function of distance from the impact point (cylindrical basalt samples 3767 and 3769).

Figure 3. Stepwise alternating field demagnetization curves for shock remanences (cylindrical basalt sample 3767). Normalized remanence intensity is plotted as a function of peak alternating field.

Figure 4. Shock remanence intensity plotted as a function of peak pressure during the shock wave propagation. Closed and open black circles denote the data of this study (cylindrical basalt sample 3767) within and beyond 3 cm from impact point, respectively. Grey circles denote the data in Sato et al. (2021).

Figure 5. Orthogonal vector plots for stepwise thermal demagnetization of shock remanence (cylindrical basalt sample 835). Closed and open symbols denote projections

for X–Y and X–Z planes, respectively.

Figure 6. Stepwise thermal demagnetization curves for shock remanences (cylindrical basalt sample 835). Normalized remanence intensity is plotted as a function of peak heating temperature.

Figure 7. Shock remanence (SRM) intensity (a) and stability (b) are plotted as a function of peak pressure during the shock wave propagation for the cylindrical basalt samples 835, 838, 839, and 840. The SRM intensity was calculated as $(J_{\mathrm{SRM}}/B_{\mathrm{SRM}})/(J_{\mathrm{ARM}}/B_{\mathrm{ARM}})$, where the J_{SRM}, J_{ARM}, B_{SRM}, and B_{ARM} are the SRM intensity, anhysteretic remanence intensity, applied field intensity in SRM experiment, and applied DC field intensity in ARM experiment. The shock remanence stability was calculated as $|\boldsymbol{J}_{\mathrm{SRM}}(6) - \boldsymbol{J}_{\mathrm{SRM}}(80)|/|\boldsymbol{J}_{\mathrm{SRM}}(2) - \boldsymbol{J}_{\mathrm{SRM}}(80)|$, where $\boldsymbol{J}_{\mathrm{SRM}}(X)$ is the SRM vector at the X mT AFD step. SRM intensity (c) and stability (d) are plotted as a function of peak pressure during the shock wave propagation for the cylindrical basalt samples 835, 836, 837, 3767, and 3773. The SRM intensity was calculated as $J_{\mathrm{SRM}}/J_{\mathrm{ARM}}$. Black and gray lines in (c) are the linear

regression and power function lines, respectively.

Figure 8. Shock remanent magnetization (SRM) intensity (a and c) and stability (b and d) are plotted as a function of peak temperature during the shock wave propagation (cylindrical basalt samples 835, 836, 837, 3767, and 3773). The SRM intensity was calculated as $|\boldsymbol{J}_{\mathrm{SRM}}(2) - \boldsymbol{J}_{\mathrm{SRM}}(80)|/|\boldsymbol{J}_{\mathrm{ARM}} - \boldsymbol{J}_{\mathrm{ARM}}(80)|$, where the $\boldsymbol{J}_{\mathrm{SRM}}$ and $\boldsymbol{J}_{\mathrm{ARM}}$ are the SRM and anhysteretic remanence vectors, respectively, and the numbers in parentheses indicate peak amplitude of alternating field demagnetization treatments. The shock remanence stability was calculated as $|\boldsymbol{J}_{\mathrm{SRM}}(6) - \boldsymbol{J}_{\mathrm{SRM}}(80)|/|\boldsymbol{J}_{\mathrm{SRM}}(2) - \boldsymbol{J}_{\mathrm{SRM}}(80)|$.

Figure 9. (a) Relationship between the experimental and model SRM intensities. (b) Differences between the experimental and model SRM intensity. Sizes of symbols indicate the magnitude of residual values.

Figure 10. (a) Amplitudes of crustal magnetic fields at an altitude of 20 projectile radius (R_{p}). Two-dimensional maps for (b) crustal remanence intensity, (c) peak pressure during

the shock wave propagation, and (d) peak temperature during the shock wave propagation. The remanence intensity of shock remanence (SRM) is normalized with respect to that of thermal remanent magnetization (TRM). The vertical and radial distances in the two-dimensional maps are normalized with respect to R_p.

[Journal of Geophysical Research: Planets]

Supporting Information for

[Pressure and temperature dependence of shock remanence intensity for single-domain titanomagnetite-bearing basalt: Toward understanding the magnetic anomalies produced by impact events]

[Masahiko Sato[1], Kosuke Kurosawa[2], Sunao Hasegawa[3], and Futoshi Takahashi[4]]

[[1]Department of Earth and Planetary Science, The University of Tokyo, Tokyo, Japan, [2]Planetary Exploration Research Center, Chiba Institute of Technology, Narashino, Japan, [3]Institute of Space and Astronautical Science, Japan Aerospace Exploration Agency, Sagamihara, Japan, [4]Department of Earth and Planetary Sciences, Kyushu University, Fukuoka, Japan]

Contents of this file

Impact simulation

We conducted shock physics modeling to calculate the peak pressure and peak temperature distributions around an impact crater using the iSALE shock physics code (Amsden et al., 1980; Ivanov et al., 1997; Wünnemann et al., 2006). We employed cylindrical coordinates, and we assumed a vertical impact of a dunite projectile onto a basaltic crust. The material model pertaining to basalt is summarized in Table S1. The impact velocity was set to 6 km s^{-1}, which corresponds to the minimum impact velocity onto Mars (Zahnle, 1993).

Because our empirical relationship cannot evaluate the effects of lithostatic pressure and geotherm, zero pressure and uniform temperature in the basaltic crust were assumed to be the initial conditions, which correspond to the craters produced on a laboratory scale. Nevertheless, our simulation may provide a qualitative understanding of the magnetic anomaly profile above the magnetized crater immediately after impact.

Since we needed to continue numerical integration until the end of a crater formation, the computational cost of this simulation is relatively high. To reduce the computational time, the spatial resolution was relatively low, and a relatively large value of gravitational acceleration was employed. The calculation settings are summarized in Table S2.

Table S1. Input parameters for the material models. Note that the parameter set pertaining to the dunite projectile and the basalt target are the same as used by Johnson et al. (2015) and Bowling et al. (2020), respectively.

EOS type	ANEOS[a]	ANEOS[a]
Material	Dunite[b]	Basalt[c]
Strength model	Rock[d]	Rock[d]
Poisson's ratio	0.25	0.25
Melting temperature (K)	1373	1360
Thermal softening parameter	1.2	0.7
Simon parameter, A (GPa)	1.52	4.5
Simon parameter, C	4.05	3.0
Cohesion (undamaged) (MPa), $Y_{coh,i}$	10	20
Cohesion (damaged) (kPa), Y_{coh}	10	10
Internal friction (undamaged), μ_{int}	1.2	1.4
Internal friction (damaged), μ_{dam}	0.6	0.6
Limiting strength (GPa), Y_{limit}	3.5	2.5
Minimum failure strain	10^{-4}	10^{-4}
Constant for the damage model	10^{-11}	10^{-11}
Threshold pressure for the damage model (MPa)	300	300

[a]Thompson and Lauson (1972), Thompson et al. (2019)
[b]Benz et al. (1989)
[c]Pierazzo et al., (2005), Sato et al. (2021)
[d]Collins et al. (2004)

Table S2. Numerical model settings.

Computational geometry	Cylindrical coordinates
Number of computational cells in the *R* direction	500
Number of computational cells in the *Z* direction	500
Number of cells for the extension zone in the *R* direction	200
Number of cells for the extension zone in the *Z* direction (top)	100
Number of cells for the extension zone in the *Z* direction (bottom)	200
Cells per projectile radius (CPPR)[b]	5
Impact velocity (km s^{-1})	6
Layer position	400 cells from the bottom of the computational domain
Artificial viscosity, a_1	0.24
Artificial viscosity, a_2	1.2

References

Amsden, A., Ruppel, H., and Hirt, C. (1980). SALE: A simplified ALE computer program for fluid flow at all speeds, Los Alamos National Laboratories Report, LA‐8095:101p.

Benz, W., Cameron, G. W., & Melosh, H. J. (1989). The origin of the Moon and the single-impact hypothesis III. Icarus, 81(1), 113–131. https:// doi.org/10.1016/0019-1035(89)90129-2

Collins, G. S., Melosh, H. J., and Ivanov, B. A. (2004). Modeling damage and deformation in impact simulations, Met. And Planet. Sci., 39, 217–231.

Ivanov, B. A., Deniem, D., and Neukum, G. (1997). Implementation of dynamic strength models into 2 ‐ D hydrocodes: Applications for atmospheric breakup and impact cratering. International Journal of Impact Engineering, 20(1−5), 411−430.

Johnson, B. C., Minton, D. A., Melosh, H. J. and Zuber, M. T. (2015). Impact jetting as the origin of chondrules. Nature 517, 339-341.

Pierazzo, E., Artemieva, N. A., Ivanov, B. A. (2005). Starting conditions for hydrothermal systems underneath Martian craters: Hydrocode modeling. in Large meteorite impacts III, eds., Kenkmann, T., Hörz, F., and Deutsch, A.,: Geological Society of America Special Paper, 384, p. 443–457.

Sato M., Kurosawa K., Kato S., Ushioda M., and Hasegawa S. (2021). Shock Remanent Magnetization Intensity and Stability Distributions of Single-Domain Titanomagnetite-Bearing Basalt Sample Under the Pressure Range of 0.1–10 GPa. Geophysical Research Letters, 48, 8.

Thompson, S. L., & Lauson, H. S. (1972). Improvements in the Chart-D radiation hydrodynamic code III: Revised analytical equation of state. pp. SC-RR-71 0714 119 pp., Sandia Laboratories, Albuquerque, NM.

Thompson, S. L., Lauson, H. S., Melosh, H. J., Collins, G. S., & Stewart, S. T. (2019, November 1). M-ANEOS (Version 1.0). Zenodo. https://doi.org/10.5281/zenodo.3525030

Wünnemann, K., Collins, G. S., and Melosh, H. J. (2006). A strain ‐ based porosity model for use in hydrocode simulations of impacts and implications for transient crater growth in porous targets. Icarus, 180(2), 514−527.

Zahnle, K., Xenological constraints on the impact erosion of the early martian atmosphere, J. Geophys. Res., 98, 10899–10913, 1993.